Elongational Flow in a Two-Dimensional Channel Geometry

B. KHOMAMI and A. J. MCHUGH, *Department of Chemical Engineering; University of Illinois, Urbana, Illinois 61801*

Synopsis

An analysis has been carried out of the two-dimensional elongational flow in an impinging channel geometry having either straight or converging wall downstream ducts. Numerical solutions for Stokes flow were obtained using a nonorthogonal transformation of variables which converts the system to a square grid geometry. Calculations show that a strong extensional flow exists from the point of channel impingement to a distance downstream approximately D/4 where D is the channel depth at the impingement point. Extensional gradients and total fluid strains also increase when the downstream duct is convergent as opposed to being straight. An experimental analysis of the velocity field in the former geometry demonstrates that, under slow flow conditions, the kinematics of a Newtonian and a highly non-Newtonian fluid become indistinguishable in the downstream region. The latter observation is shown to be consistent with second-order fluid theory and the Giesekus-Tanner Theorem.

INTRODUCTION

The importance of elongational flow fields in the processing of high-strength crystalline polymer fibers and films is well known. Extensional stresses uncoil and orient macromolecules, leading to the formation of structures which, upon subcooling, crystallize either as shish-kebab fibers (from solution) or core crystals with epitaxially grown lamellae (from the melt). Both the magnitude of the velocity gradient and the total strain are measures of the potential for molecular orientation in such flows. A number of studies have therefore focused on the use of controlled extensional flows to analyze orientation effects and flow history-morphology-property interactions in crystallizable systems. In most cases, converging flow geometries have been employed which unfortunately produce nonideal kinematics in the sense that they are Lagrangian unsteady. On the other hand, such systems have the important feature that flow is continuous, thus allowing direct analysis of the morphology-property characteristics of the fiber or film extrudate.[1,2]

Recently, Cressely and Hocquart have investigated a series of flows of the impinging jets type,[3] and in one particular case, illustrated what is essentially a reverse bifurcation flow geometry consisting of two slanted channels impinging to form a single downstream channel. Observations of the flow birefringence indicated that a highly elongational field exists near the channel bifurcation insert. However, to our knowledge, no corresponding analysis or kinematic study has been reported. The two-dimensional nature of this flow makes it attractive to consider as a processing geometry since experimental and numerical analysis (at least for Stokes flows) are more tractable. Furthermore, since the high stretch rates near the bifurcation tip can be enhanced by

Journal of Applied Polymer Science, Vol. 33, 1495–1509 (1987)
 CCC 0021-8995/87/051495-15$04.00

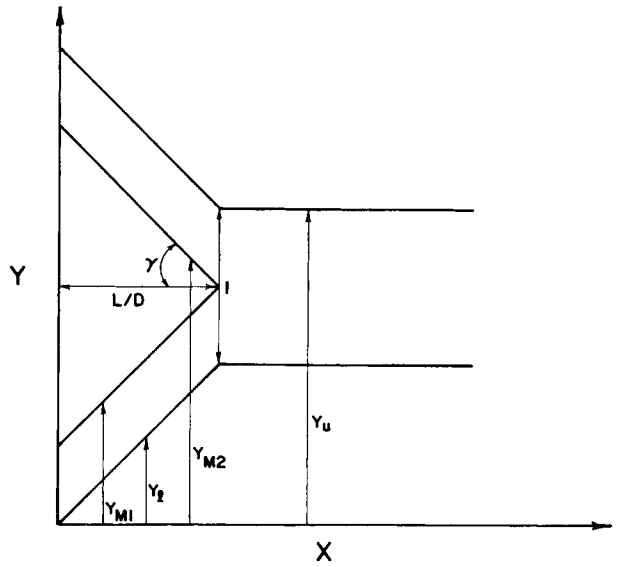

Fig. 1. Impinging channel flow geometry with straight wall downstream duct.

downstream tapering of the flow channel, one has the possibility of increased total strains. For these reasons we have carried out an analysis of this geometry, a discussion of which is presented in the following sections. We begin first with a numerical solution of the Stokes flow problem.

STOKES FLOW EQUATIONS AND ANALYSIS

Figures 1 and 2 show the flow geometries which were considered in this study. Since, to our knowledge, closed-form analytic solutions are not available, a finite-difference numerical scheme was used to analyze the steady motion of a Newtonian fluid in Stokes flow in these geometries. Our numerical scheme utilizes a modification of a nonorthogonal transformation, originally described by Clark and co-workers,[4,5] which shifts the coordinates to a square mesh field. In consequence, the irregularity of the geometry is introduced into the governing equations. The transformed coordinates η—ξ are related to the nondimensional X, Y coordinates of the original flow field by the following general equations.

$$\text{Trunk:} \qquad \eta = \frac{Y - Y_\ell}{Y_u - Y_\ell} \tag{1}$$

$$\text{Lower branch:} \qquad \eta = \eta_o \frac{Y - Y_\ell}{Y_{m1} - Y_\ell} \tag{2}$$

$$\text{Upper branch:} \qquad \eta = \eta_o + \frac{Y - Y_{m2}}{Y_u - Y_{m2}}(1 - \eta_o) \tag{3}$$

$$\xi = X \tag{4}$$

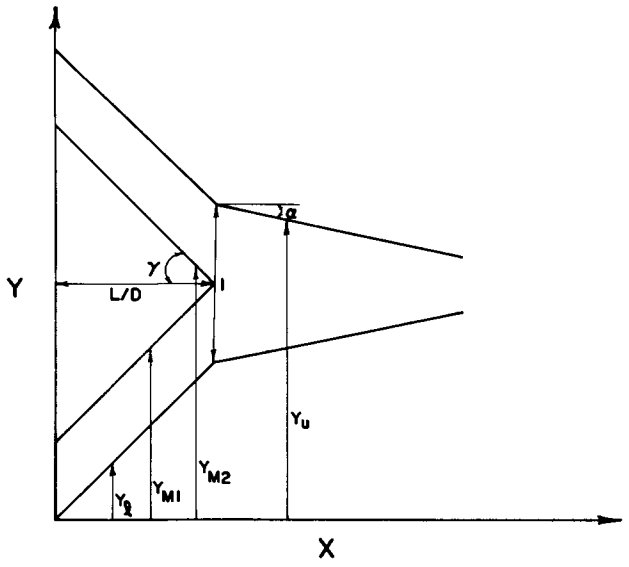

Fig. 2. Impinging channel geometry with converging wall downstream duct.

In these equations, subscripts ℓ, u, $m1$, $m2$ identify the lower, upper, mid lower, and mid upper boundaries, respectively, and X and Y are the position coordinates which have been nondimensionalized with respect to the channel depth, D, at the insert point (see Figs. 1 and 2).

The parameter η_o is defined as:

$$\eta_o = \frac{Y_{m1} - Y_\ell}{Y_u - Y_\ell} \tag{5}$$

and defines the location of the insert; for flows with equal upper and lower branches this value will be 1/2.

Figure 3, shows both geometries in the transformated coordinate space which serves as the calculation coordinates for the numerical scheme.

The governing equations for the velocity components $v_x(x, y)$ and $v_y(x, y)$ in the x and y directions are the two-dimensional Stokes equations and the continuity equation:

$$0 = \frac{-1}{\rho}\frac{\partial P}{\partial x} + \nu\left(\frac{\partial^2 v_x}{\partial x^2} + \frac{\partial^2 v_x}{\partial y^2}\right) \tag{6}$$

$$0 = \frac{-1}{\rho}\frac{\partial P}{\partial y} + \nu\left(\frac{\partial^2 v_y}{\partial x^2} + \frac{\partial^2 v_y}{\partial y^2}\right) \tag{7}$$

$$0 = \frac{\partial v_x}{\partial x} + \frac{\partial v_y}{\partial y} \tag{8}$$

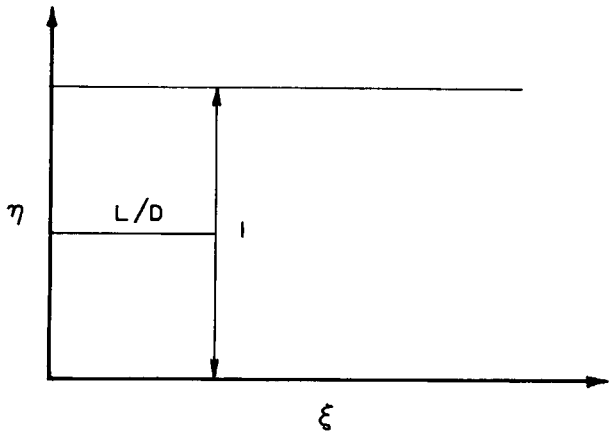

Fig. 3. Transformed geometries of Figures 1 and 2.

Following standard procedures[6] these can be written in terms of the stream function $\bar{\psi}$ and the vorticity $\bar{\zeta}$ to give

$$\nabla^2\bar{\psi} = -\bar{\zeta} \tag{9}$$

$$\nabla^2\bar{\zeta} = 0 \tag{10}$$

Transformation to $\zeta - \eta$ coordinates gives the following equation set

$$\left(\frac{\partial\xi}{\partial X}\right)^2\frac{\partial^2\zeta}{\partial\xi^2} + 2\frac{\partial\xi}{\partial X}\frac{\partial\eta}{\partial X}\frac{\partial^2\zeta}{\partial\xi\,\partial\eta} + \left[\left(\frac{\partial\eta}{\partial Y}\right)^2 + \left(\frac{\partial\eta}{\partial X}\right)^2\right]\frac{\partial^2\zeta}{\partial\eta^2}$$

$$+\left[\frac{\partial^2\eta}{\partial X^2} + \frac{\partial^2\eta}{\partial Y^2}\right]\frac{\partial\zeta}{\partial\eta} + \frac{\partial^2\xi}{\partial X^2}\frac{\partial\zeta}{\partial\xi} = 0 \tag{11}$$

$$\left(\frac{\partial\xi}{\partial X}\right)^2\frac{\partial^2\psi}{\partial\xi^2} + 2\frac{\partial\xi}{\partial X}\frac{\partial\eta}{\partial X}\frac{\partial^2\psi}{\partial\xi\,\partial\eta} + \left[\left(\frac{\partial\eta}{\partial Y}\right)^2 + \left(\frac{\partial\eta}{\partial X}\right)^2\right]\frac{\partial^2\psi}{\partial\eta^2}$$

$$+\left[\frac{\partial^2\eta}{\partial X^2} + \frac{\partial^2\eta}{\partial Y^2}\right]\frac{\partial\psi}{\partial\eta} + \frac{\partial^2\xi}{\partial X^2}\frac{\partial\psi}{\partial\xi} = -\zeta \tag{12}$$

In these expressions all variables are nondimensional and are defined as: $\psi = \bar{\psi}/\nu$, $\zeta = D^2\bar{\zeta}/\nu$, $X = x/D$ and $Y = y/D$ where ν is the kinematic viscosity. In order to write the governing equations in terms of ξ and η, the derivatives $\partial\xi/\partial X$, $\partial\eta/\partial X$, $\partial\eta/\partial Y$, $\partial^2\eta/\partial X^2$, $\partial^2\eta/\partial Y^2$ must be evaluated for each section. The final equations for the straight downstream channel (Fig.

1) become the following:

Trunk:

$$\frac{\partial^2\zeta}{\partial\xi^2} + \frac{\partial^2\zeta}{\partial\eta^2} = 0 \tag{13}$$

$$\frac{\partial^2\psi}{\partial\xi^2} + \frac{\partial^2\psi}{\partial\eta^2} = -\zeta \tag{14}$$

Lower branch:

$$\frac{\partial^2\zeta}{\partial\xi^2} - 2(\tan\gamma)\frac{\partial^2\zeta}{\partial\xi\,\partial\eta} + (\tan^2\gamma + 1)\frac{\partial^2\zeta}{\partial\eta^2} = 0 \tag{15}$$

$$\frac{\partial^2\psi}{\partial\xi^2} - 2(\tan\gamma)\frac{\partial^2\psi}{\partial\xi\,\partial\eta} + (\tan^2\gamma + 1)\frac{\partial^2\psi}{\partial\eta^2} = -\zeta \tag{16}$$

Upper branch:

$$\frac{\partial^2\zeta}{\partial\xi^2} + 2(\tan\gamma)\frac{\partial^2\zeta}{\partial\xi\,\partial\eta} + (\tan^2\gamma + 1)\frac{\partial^2\zeta}{\partial\eta^2} = 0 \tag{17}$$

$$\frac{\partial^2\psi}{\partial\xi^2} + 2(\tan\gamma)\frac{\partial^2\psi}{\partial\xi\,\partial\eta} + (\tan^2\gamma + 1)\frac{\partial^2\psi}{\partial\eta^2} = -\zeta \tag{18}$$

For the converging downstream channel (Fig. 2) the equations for the trunk become

$$\frac{\partial^2\zeta}{\partial\xi^2} + \left[2\frac{2\tan(\alpha)Y - \tan\alpha - 2\tan\gamma\tan\alpha}{(1 - 2(\xi-1)\tan\alpha)^2}\right]\frac{\partial^2\zeta}{\partial\xi\,\partial\eta} + \left[\left(\frac{2\tan(\alpha)Y - \tan\alpha - 2\tan\gamma\tan\alpha}{(1 - 2(\xi-1)\tan\alpha)^2}\right)^2 + \left(\frac{1}{1 - 2(\xi-1)\tan\alpha}\right)^2\right]\frac{\partial^2\zeta}{\partial\eta^2} + \left[4\tan(\alpha)\frac{[2\tan(\alpha)Y - \tan\alpha - 2\tan\gamma\tan\alpha]}{[1 - 2(\xi-1)\tan\alpha]^3}\right]\frac{\partial\zeta}{\partial\eta} = 0 \tag{19}$$

and

$$\frac{\partial^2\psi}{\partial\xi^2} + \left[2\frac{2\tan(\alpha)Y - \tan\alpha - 2\tan\gamma\tan\alpha}{(1 - 2(\xi-1)\tan\alpha)^2}\right]\frac{\partial^2\psi}{\partial\xi\,\partial\eta} + \left[\left(\frac{2\tan(\alpha)Y - \tan\alpha - 2\tan\gamma\tan\alpha}{(1 - 2(\xi-1)\tan\alpha)^2}\right)^2 + \left(\frac{1}{1 - 2(\xi-1)\tan\alpha}\right)^2\right]\frac{\partial^2\psi}{\partial\eta^2} + \left[4\tan\alpha\frac{[2\tan(\alpha)Y - \tan\alpha - 2\tan\gamma\tan\alpha]}{[1 - 2(\xi-1)\tan\alpha]^3}\right]\frac{\partial\psi}{\partial\eta} = -\zeta \tag{20}$$

The upper and lower branch equations are identical to those of the straight channel geometry.

The flow field is prescribed by the wall boundary conditions on ψ and ζ and by the inlet and outlet conditions. The stream function boundary conditions are:

$$\psi = 0 \quad \text{at} \quad \eta = 0 \tag{21}$$

$$\psi = \text{volumetric flowrate } (Q) \text{ at } \quad \eta = 1 \tag{22}$$

$$\psi = \frac{Q}{2} \quad \text{at} \quad \eta = \frac{1}{2} \quad \text{for} \quad 0 \le \xi \le \frac{L}{D} \tag{23}$$

For the vorticity at the wall the following approximation can be used,[6] the suitability of which was evaluated in straight channel flow calculations.

$$\zeta_{i,\omega} = \frac{2(\psi_{i,\omega} - \psi_{i,\omega+1})}{\Delta Y^2} + O(\Delta Y) \tag{24}$$

Here ω signifies the position on the wall. However, for the sharp corner of the insert this expression is not adequate hence there we assume $\zeta = 0$.

The inlet and outlet are considered to be far enough from the insert tip to be free of any nonuniform flow effects and both conditions are prescribed to be parabolic profiles. Thus for the lower branch

$$\zeta = -2G\left[(\eta + (\tan\gamma)\xi)\cos\gamma - \xi\sin\gamma - \frac{\cos\gamma}{4}\right] \tag{25}$$

$$\psi = G\cos\gamma\left[\frac{\left((\eta + (\tan\gamma)\xi)\cos\gamma - \xi\sin\gamma + \dfrac{\cos^3\gamma}{4} + \dfrac{\cos\gamma\sin^2\gamma}{4} - \dfrac{\cos\gamma}{2}\right)^3}{3\cos\gamma} - \left(\frac{\cos\gamma}{4}\right)^2(\eta + (\tan\gamma)\xi)\right] + c \tag{26}$$

while for the upper branch, the following hold:

$$\zeta = -2G\left[(\eta + 2\tan\gamma - (\tan\gamma)\xi)\cos\gamma + \xi\sin\gamma - \frac{\cos^3\gamma}{4} - \frac{\cos\gamma\sin^2\gamma}{4} - 2\sin\gamma - \frac{\cos\gamma}{2}\right] \tag{27}$$

$$\psi = G\cos\gamma\left[\left((\eta + 2\tan\gamma - (\tan\gamma)\xi)\cos\gamma + \xi\sin\gamma - \frac{\cos^3\gamma}{4} - \frac{\cos\gamma\sin^2\gamma}{4} - 2\sin\gamma - \frac{\cos\gamma}{2}\right)^3 \Big/ 3\cos\gamma\right] - \left(\frac{\cos\gamma}{4}\right)^2(\eta + 2\tan\gamma - (\tan\gamma)\xi) + c \tag{28}$$

where c and G are determined based on the volumetric flow rate.

The outlet conditions for the converging downstream channel and straight channels differ. Assuming Hamel flow for the converging channel one obtains the following

$$\zeta = \frac{2G \sin\left(2 + \tan^{-1}\left(\dfrac{Y - 1.5}{3.5137 - X}\right)\right)}{(3.5137 - X)^2 + (Y - 1.5)^2} \tag{29}$$

$$\psi = G\left(\frac{\sin\left[2\tan^{-1}\left(\dfrac{Y - 1.5}{3.5137 - X}\right)\right]}{2} - \cos 2\alpha \tan^{-1}\left(\frac{Y - 1.5}{3.5137 - X}\right)\right) + c \tag{30}$$

For the straight channel downstream one instead has

$$\zeta = -2G(\eta + \tan\gamma - 1.5) \tag{31}$$

$$\psi = G\left[\frac{(\eta + \tan\gamma - 1.5)^3}{3} - \left(\frac{1}{2}\right)^2(\eta + 1)\right] + c \tag{32}$$

where G and c are constants which depend on the flow rate.

Since we have a square mesh for the numerical computation field, central difference forms of the vorticity and stream function equations were employed using a mesh size equal to 1/40 of the characteristic length D. For the vorticity equations, implicit solutions of the finite difference forms were carried out using the steady Liebman method.[6] Solution of the stream function equations required an under relaxation method using relaxation parameters which decreased with the interation number to avoid instabilities. The convergence criterion was the following:

$$\left|\frac{\psi_{ij}^{k+1} - \psi_{ij}^{k}}{\psi_{ij}^{k}}\right| < 0.01 \tag{33}$$

where k is the iteration number.

NUMERICAL RESULTS AND DISCUSSION

The streamline pattern for flow in a channel configuration corresponding to a 45° bifurcation insert and a straight wall downstream duct is shown in Figure 4. The effect of a converging downstream flow with a channel convergence angle of $\gamma/4$ (i.e., 11.25°) is shown in Figure 5. The velocity gradient tensor $[(\nabla \mathbf{v})^T]_{ij} = \partial v_i/\partial x_j$ for either system can be written as

$$(\nabla \mathbf{v})^T = \frac{\nu}{D^2}\begin{pmatrix} \dfrac{\partial^2\psi}{\partial X\,\partial Y} & \dfrac{\partial^2\psi}{\partial X^2} \\ -\dfrac{\partial^2\psi}{\partial Y^2} & -\dfrac{\partial^2\psi}{\partial X\,\partial Y} \end{pmatrix} \tag{34}$$

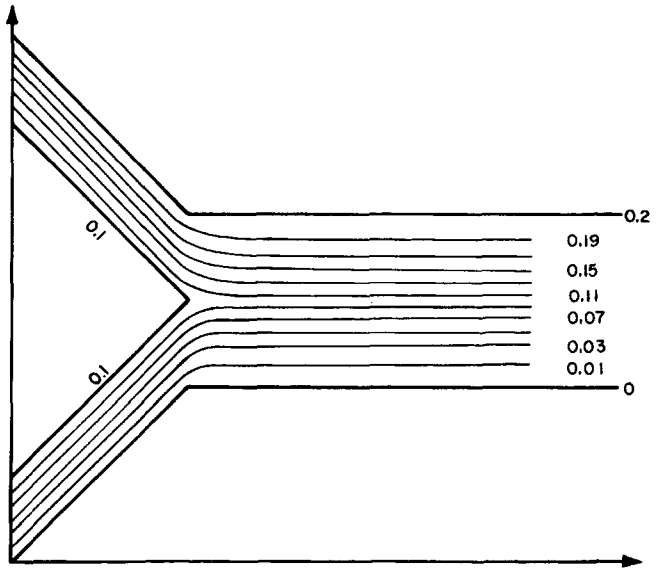

Fig. 4. Calculated streamline pattern for straight wall geometry with 45° channel insert.

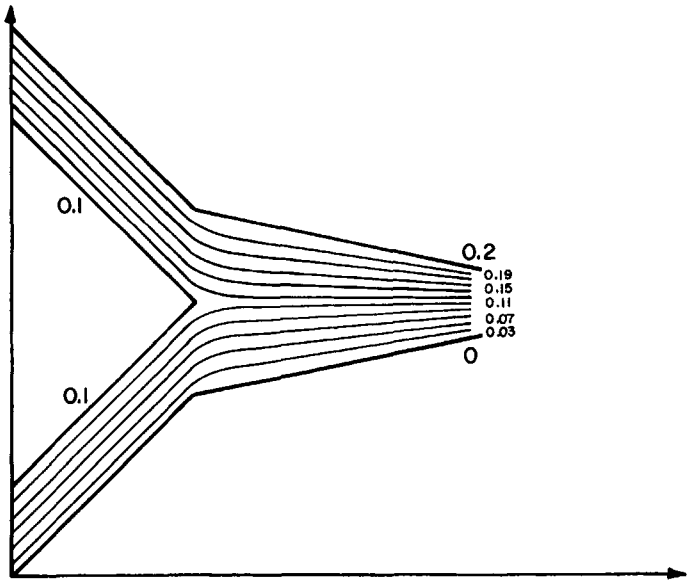

Fig. 5. Calculated streamline pattern for converging wall geometry with $\alpha = 11.25°$.

In most cases the kinematics were nearly planar elongational, in that the off-diagonal terms were negligible compared to the diagonal components. Comparisons of the elongation rate, $\partial v_x/\partial x$, for the two geometries are shown in Figures 6 and 7 as functions of channel position downstream from the insert tip for a gap width of 1 cm. One sees that the extension rate is clearly enhanced by the tapered channel. The effects of branch angle, γ, and convergence angle, α on the centerline extensional gradient are illustrated in Figure

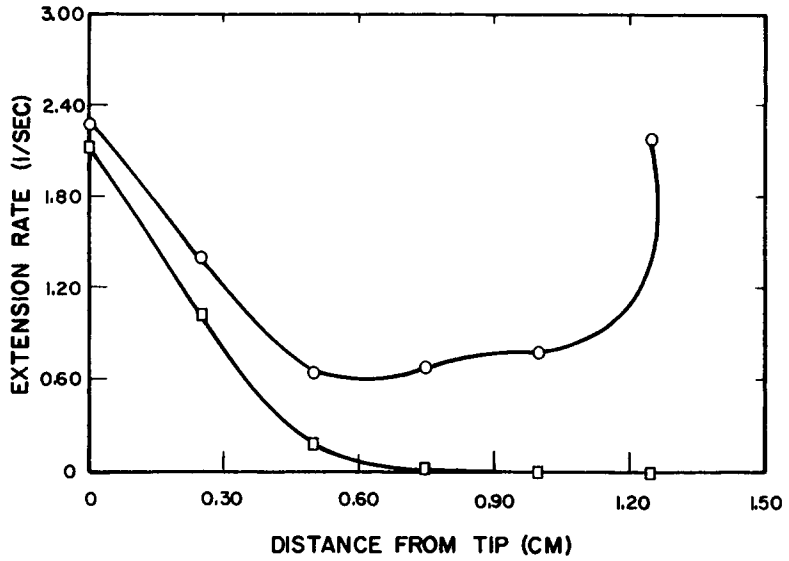

Fig. 6. Centerline extensional gradient as a function of distance downstream for converging (○) and straight wall (□) geometries.

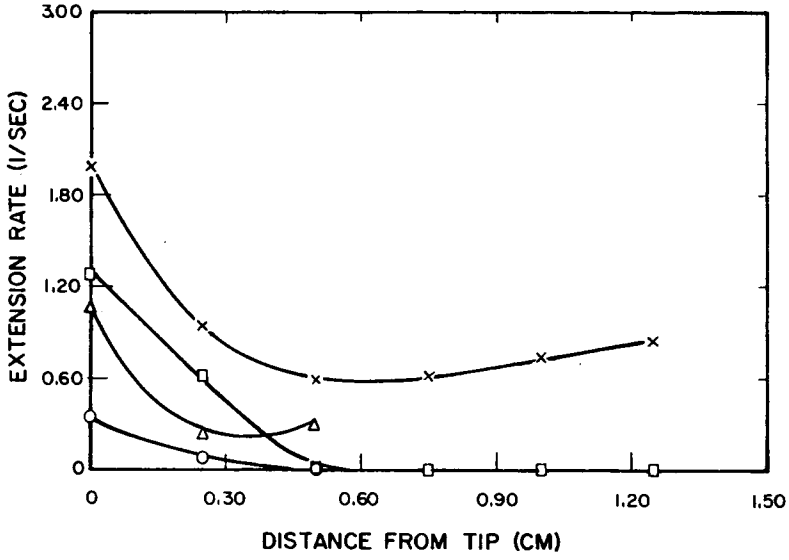

Fig. 7. Extensional gradient dependence with distance for converging (×, △) and straight wall (□, ○) geometries (×, □) = 0.1 D from centerline, (△, ○) = 0.2 D from centerline.

8. Comparing Figure 6 with the solid line of Figure 8 one sees that, as expected, at a fixed convergence angle, the initial extension rate increases with increased branch angle. However, once the downstream converging flow becomes fully developed, the resulting gradient depends only upon the convergence angle. Since from Eq. (34), strain rate also varies as $1/D^2$, then for a given outlet gap and overall pressure drop, a particular combination of D and α should lead to an optimal strain rate.

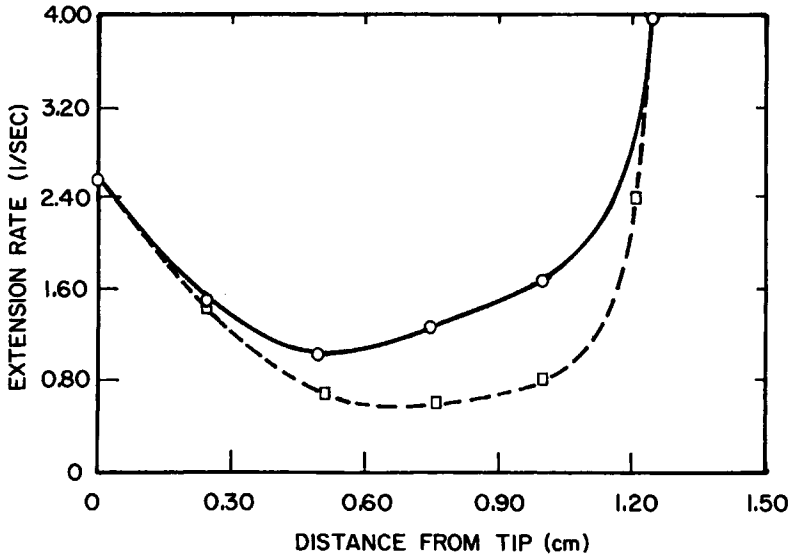

Fig. 8. Effect of convergence angle, $\alpha = 15°$ (○) and 11.25° (□) on centerline extensional gradient for 70° branch angle, γ.

The effect of stream impingement dissipates about 0.75 D downstream from the insert as can also be seen in Figures 6 and 7. Thus, the impinging channels give rise to a high extension rate near the bifurcation point, while the converging flow leads to extension rates which are highest near the exit. In consequence, the total extensional strain along the symmetry axis of the converging channel section is effectively increased by the upstream geometry. Estimating the strain by the product of residence time with twice the extension rate, one finds an increase over the case of simple converging flow by a factor of about 1.7.

EXPERIMENTAL OBSERVATIONS

To further evaluate the nature of the extensional flow in this geometry, a series of experiments was carried out using the channel design shown in Figure 9. Streak photography was used to obtain the flow kinematics in the down-

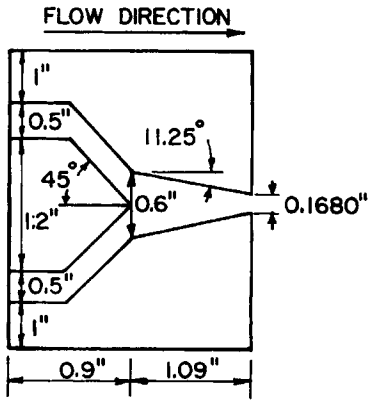

Fig. 9. Sketch of experimental test section with dimensions.

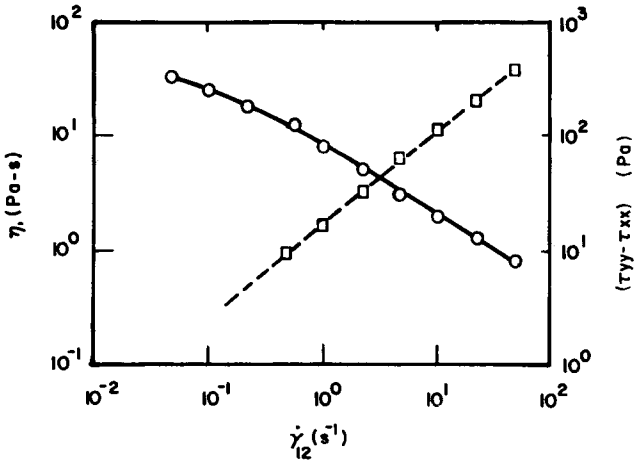

Fig. 10. Viscosity and first normal stress difference versus shear rate for polyacrylamide solution at 26° C.

stream section for two fluids, one a Newtonian 96% glycerin-water mixture, the other a highly non-Newtonian solution of 1 wt% polyacrylamide (Separan AP-30) in a 50% glycerine-water mixture. The flow loop, optical system, and data analysis methods were the same as those described in detail elsewhere.[7] Viscosity and normal stress data for the polymer solution were obtained using a Rheometrics System 4 with a cone and plate assembly. The flow curve is shown in Figure 10.

Figures 11 to 13 show representative plots of the measured velocity profiles at various axial positions downstream from the insert tip. The solid lines are based on numerical calculations and the broken lines are calculations based on

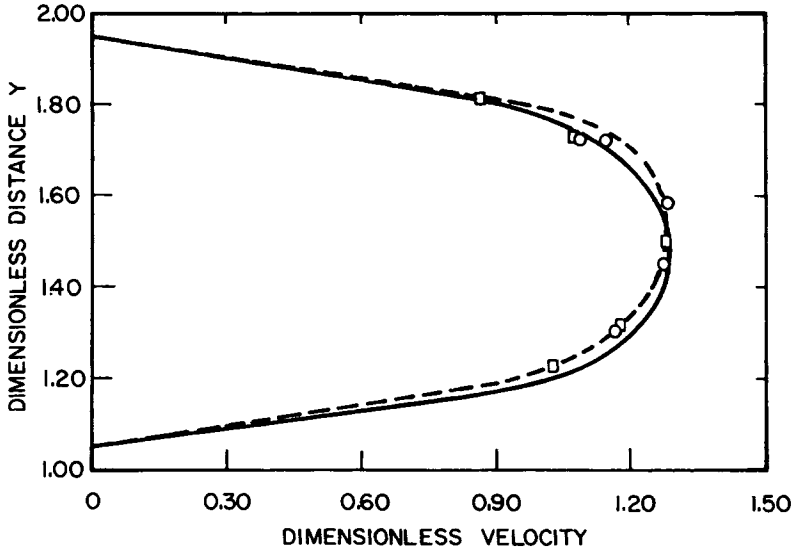

Fig. 11. Measured velocity profile at $x = 0.25\ D$ for Newtonian (□) and polyacrylamide (○) systems --- numerically calculated profile; —profile corresponding to power law flow (lubrication approximation).

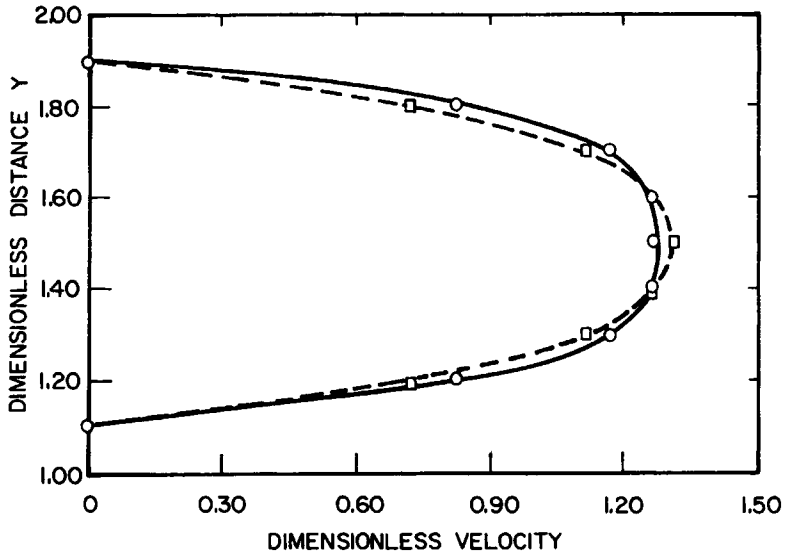

Fig. 12. Measured and calculated velocity profiles at x = 0.50 D. Same symbols as Fig. 11.

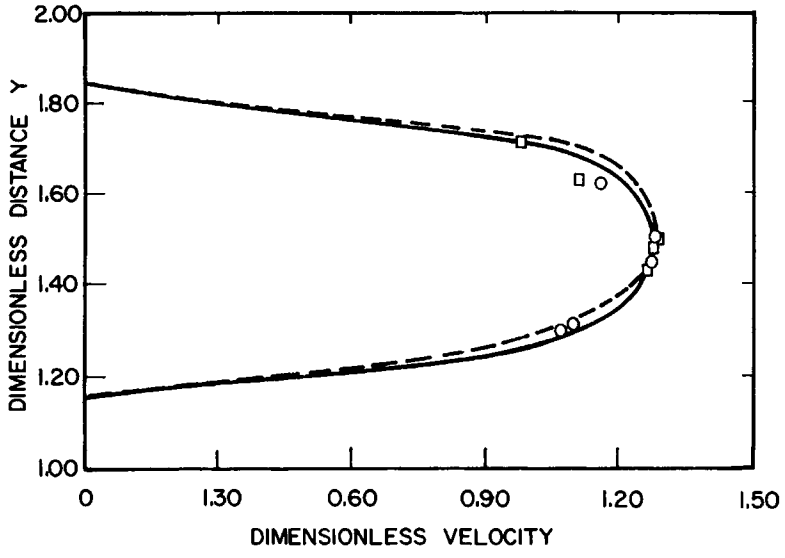

Fig. 13. Measured and calculated velocity profiles at x = 0.75 D. Same symbols as Fig. 11.

the lubrication assumption for power law flow in the tapered section using a power law index n = 0.38 which results from Figure 10. In all cases the velocities have been nondimensionalized with respect to the average velocity at the points in question and distances have been normalized with respect to the channel depth, D. The pattern displayed by these data is similar to an earlier observation[7] in that, to within experimental error, the profiles of the two fluids are essentially indistinguishable and both agree well with the Newtonian calculation. In the latter case, Mackay and McHugh used a two-dimensional converging-plates geometry and flow past a slender body to

investigate the nature of the enhancements in extension rates which occur near the body tip. Their velocity field data showed that in regions immediately downstream from the seed symmetry axis, the kinematics for Newtonian and non-Newtonian systems were essentially indistinguishable, though in the macroscopic field they differed significantly. Using the flow classification method suggested by Tanner[8] for motions with constant stretch history, they concluded that the local flow was strong and that under such conditions the kinematics of different fluids become similar. In the present case we believe the similarity of our macroscopic profiles may simply be a reflection of slow flow behavior which can be rationalized by means of the Giesekus-Tanner Theorem.[9] Following standard arguments[10] one can show that in slowly varying flows, the general viscoelastic constitutive equation from simple fluid theory becomes equivalent to a perturbation series about Newtonian behavior, the first two terms of which give the well-known second-order fluid constitutive equation for the extra stress, τ, as

$$\tau = \eta_o \Delta^{(1)} - \left(\frac{\Psi_1}{2}\right)\Delta^{(2)} + \Psi_2 \Delta^{(1)} \cdot \Delta^{(1)} \tag{35}$$

In these expressions, η_o is the Newtonian viscosity, Ψ_1 and Ψ_2 are the (constant) first and second normal stress coefficients and the $\Delta^{(i)}$ are the first and second Rivlin-Ericksen tensors given, respectively, by the deformation rate ($\Delta^{(1)}$) and the convected Oldroyd derivative of the deformation rate ($\Delta^{(2)}$). Inspection of the rheological data in Figure 10 shows that the variation in viscosity is less than 5% between 4×10^{-2} s^{-1} and 8×10^{-2} s^{-1}, which corresponds to the shear rates in our geometry near the center line (i.e., from the center line to about half the distance to either wall). Likewise, Ψ_1 changes less than about 7% in this range. Thus, one could argue that the fluid behavior is essentially that of the second-order model under these conditions. The Giesekus-Tanner theorem states that for any plane creeping flow, the Newtonian velocity field, for given boundary conditions will also be a solution for the second-order fluid flow. Hence, one would expect to see a behavior pattern essentially as shown in Figures 11–13.

The second-order fluid assumption further enables computation of normal stresses for our flow from the following expressions[9]

$$\begin{aligned}\tau_{xx} = {} & 2\eta_o \bar{\psi}_{xy} - (\beta_2 - \beta_{11})\left[4\bar{\psi}_{xy}^2 + \left(\bar{\psi}_{xx} - \bar{\psi}_{yy}\right)^2\right] \\ & + \beta_2\left[2\left(\bar{\psi}_y \bar{\psi}_{xxy} - \bar{\psi}_x \bar{\psi}_{xyy}\right) + \left(\bar{\psi}_{xx}^2 - \bar{\psi}_{yy}^2\right)\right]\end{aligned} \tag{36}$$

$$\begin{aligned}\tau_{yy} = {} & -2\eta_o \bar{\psi}_{xy} - (\beta_2 - \beta_{11})\left[4\bar{\psi}_{xy}^2 + \left(\bar{\psi}_{xx} - \bar{\psi}_{yy}\right)^2\right] \\ & + \beta_2\left[2\left(\bar{\psi}_x \bar{\psi}_{xyy} - \bar{\psi}_y \bar{\psi}_{xxy}\right) + \left(\bar{\psi}_{yy}^2 - \bar{\psi}_{xx}^2\right)\right]\end{aligned} \tag{37}$$

where $\beta_2 = -\Psi_1/2$ and $\beta_{11} = \Psi_2$. The usual shorthand notation has also been used to write the partial derivatives of $\bar{\psi}$ as subscripts. In order to evaluate the stress terms, differentiation of the numerically generated stream functions

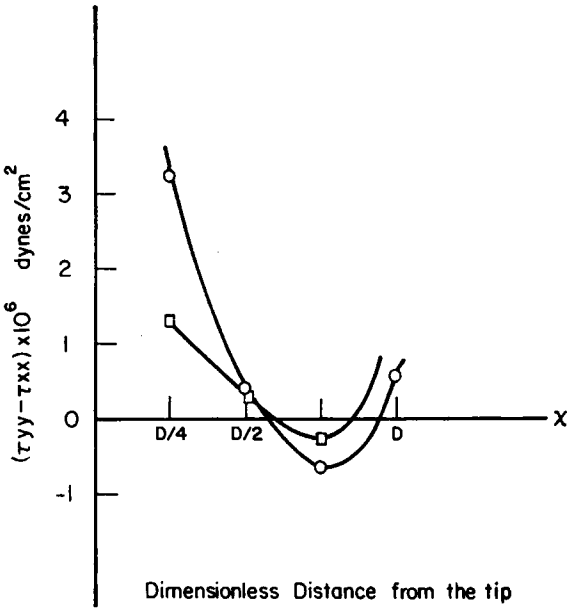

Fig. 14. First normal stress difference (○) calculated from Eqs. (36) and (37) for the geometry of Fig. 9 compared to calculations of Ref. 11 (□) for a simple converging channel.

is necessary which, together with the small magnitude of $\bar{\psi}(0 \rightarrow 0.2)$ greatly reduces the accuracy of the computations. Furthermore, very small values of the derivatives are multiplied by orders-of-magnitude larger coefficients (i.e., η_o, β_2, β_{11}) in these equations, hence introducing large uncertainty in the calculation. For distances smaller than $D/4$ from the bifurcation insert, gradient changes grow rapidly, hence higher order terms would be needed in the stress equations and the Giesekus-Tanner theorem would no longer apply. Thus, with these limitations in mind, the normal stresses τ_{xx} and τ_{yy} were computed for the region a distance $D/4$ downstream from the insert to the channel exit and are shown in Figure 14 as a first normal stress difference. These calculations can be compared with those given by Han and Drexler[11] for flow into a converging channel. For our system the effect of the impinging stream entrance flow dissipates at distances on the order of 0.75 D from the insert and one sees a pattern similar to theirs in that normal stress effects become dominated by the converging channel kinematics. On the other hand, up to that point, flow will be dominated by the strong extensional kinematics generated by the impinging streams, thus normal forces become much larger.

Future studies will address stress measurements using flow birefringence with crystallizable systems to determine whether and how much oriented structure formation can be affected in such a geometry. For the present, however, we feel that the potential of this geometry for extensional flow studies has been demonstrated.

This work has been supported in part under a grant from the National Science Foundation through the Materials Research Laboratory of the University of Illinois Grant DMR 83-16981.

References

1. D. H. Crater and J. A. Cuculo, *J. Polym. Sci. Phys.* Ed., **21**, 2219 (1983).
2. S. L. Sakellarides and A. J. McHugh, *Polym. Eng. Sci.*, **25**, 1179 (1985).
3. R. Cressely and R. Hocquart, *Optica Acta*, **27**, 699 (1980).
4. M. E. Clark, J. M. Robertson, and L. C. Cheng, *Proc. Symp. Computer Methods in Engineering*, Vol 1, Univ. Southern Calif., Aug. 1977, p. 497.
5. L. C. Cheng, M. E. Clark, J. M. Robertson, and N. H. Chao, in *First Mid-Atlantic Conference on Bio-Fluid Mechanics*, Ed. D. J. Schneck, Virg. Poly. Tech. Inst., Blacksburg, VA, 1978, p. 151.
6. P. J. Roache, *Computational Fluid Dynamics*, Hermosa, Albuquerque, 1972.
7. M. E. Mackay and A. J. McHugh, *J. Rheol.*, **29**, 655 (1985).
8. R. I. Tanner, *AIChE J.*, **22**, 910 (1976).
9. R. I. Tanner, *Phys. Fluids*, **9**, 1246 (1968); H. Giesekus, *Rheol. Acta*, **3**, 59 (1963).
10. R. B. Bird, R. C. Armstrong, and O. Hassager, *Dynamics of Polymeric Liquids*, vol 1, Wiley, New York (1977).
11. C. D. Han and L. R. Drexler, *J. Appl. Polym. Sci.*, **17**, 2369 (1973).

Received May 22, 1986
Accepted September 4, 1986